ELSEVIER

Powder Technology 90 (1997) 115–123

POWDER TECHNOLOGY

An engineering model for dilute riser flow

J.J. Nieuwland, E. Delnoij, J.A.M. Kuipers *, W.P.M. van Swaaij

Twente University, PO Box 217, 7500 AE Enschede, Netherlands

Received 15 May 1995; revised 22 June 1996

Abstract

To facilitate understanding of the hydrodynamic behaviour of CFBs, a one-dimensional model for the riser tube of a CFB has been developed. The model describes steady state hydrodynamic key variables (i.e. cross-sectional averaged values of pressure, solids concentration and velocities of both phases) for developing axi-symmetrical flow as a function of the axial position in the riser tube. Calculated results have been compared with experimental data obtained from a small scale CFB unit which could be operated at pressures up to 6 bar. Despite the simplicity of the model, it turned out that the model was capable of predicting the effect of changes in operating conditions (i.e. gas velocity, solids mass flux, operating pressure and particle diameter). The model neglects the existence of clustering of particles, lateral solids segregation and solids downflow near the tube wall, which limits the applicability to dilute systems ($\epsilon_s < 0.04$).

Keywords: One-dimensional model; Steady state hydrodynamics; Operating conditions; Axi-symmetrical flow; Dilute systems

1. Introduction

Circulating fluidized beds possess a complex flow structure, which hampers industrial application despite their advantageous properties such as excellent heat and mass transfer characteristics between gas and solid phase, control of solids concentration and continuous operation. During the last decades several models have been proposed to describe the complex hydrodynamics of circulating fluidized beds (CFBs). Most of these models have an empirical base which makes them appropriate engineering tools within restricted flow regimes and for specific CFB configurations. In this work a brief summary is given of the models proposed in the literature to describe the hydrodynamic behaviour in an axial direction. Subsequently, the calculated results are compared thoroughly with the experimental data obtained in a steel CFB configuration that can be operated to pressures up to 6 bar.

2. Model equations

2.1. Governing equations

The governing equations can be obtained from the general two-fluid model equations presented by Kuipers et al. [1] by integrating with respect to the radial coordinate of the stationary mass and momentum conservation equations for both the gas and solids phase. As a consequence, the variables in the resulting equations can be interpreted as averages over the tube radius. The reduced conservation equations for mass and momentum are given for both the gas and solid phase.

Continuity equation—gas phase:

$$\frac{\mathrm{d}(\epsilon_f \rho_f u)}{\mathrm{d}z} = 0 \tag{1}$$

Continuity equation—solid phase:

$$\frac{\mathrm{d}(\epsilon_s \rho_s v)}{\mathrm{d}z} = 0 \tag{2}$$

Momentum equation—gas phase in z-direction:

$$\frac{\mathrm{d}(\epsilon_f \rho_f u^2)}{\mathrm{d}z} = -\epsilon_f \frac{\mathrm{d}P}{\mathrm{d}z} - \beta(u - v) + \epsilon_f \rho_f g_z + F_{f,\,\mathrm{wall}} \tag{3}$$

Momentum equation—solid phase in z-direction:

$$\frac{\mathrm{d}(\epsilon_s \rho_s v^2)}{\mathrm{d}z} = -\epsilon_s \frac{\mathrm{d}P}{\mathrm{d}z} + \beta(u - v) + \epsilon_s \rho_s g_z + F_{s,\,\mathrm{wall}} \tag{4}$$

In the momentum equations $F_{f,\,\mathrm{wall}}$ and $F_{s,\,\mathrm{wall}}$ represent, respectively, the wall friction forces acting on the gas and solid phase per m^3 gas–solid mixture. Viscous momentum transport in the axial direction has been neglected for both phases because for riser flow convective axial momentum

* Corresponding author.

PII S0032-5910(96)03205-6

transport dominates viscous momentum transport in axial direction.

From the model equations, Eqs. (1)–(4), listed here, the following expression for the total pressure gradient can be derived:

$$-\frac{dP}{dz}=G_f\frac{du}{dz}-\epsilon_f\rho_f g_z-F_{f,\,wall}+G_s\frac{dv}{dz}-\epsilon_s\rho_s g_z-F_{s,\,wall} \tag{5}$$

From this equation, it can be concluded that the pressure gradient balances the net force per unit volume gas–solid mixture arising from acceleration, gravity and wall friction for both phases.

Systems in which high gas velocities and low solids concentrations prevail, i.e. risers which operate in the pneumatic transport regime, the dominant contribution to the pressure gradient is wall friction. In this regime an increase in gas velocity, at constant solids mass flux G_s, results in increasing pressure gradient. In contrast, there are systems characterized by high solids concentrations, the so-called fast fluidization regime [2], in which the gravity force acting on the solids determines the magnitude of the pressure gradient. In this regime, an increase in gas velocity at constant solids mass flux results in a decrease in pressure gradient, which can be attributed to a decrease in solids concentration.

Eqs. (1) to (4) can be solved if constitutive relations are specified, that express the unknown parameters as a function of the primary variables ϵ_f, P, u and v.

2.2. Constitutive relations

2.2.1. Densities of both phases

The gas phase is considered as a compressible medium, where the ideal gas law can be used to relate gas phase density to pressure:

$$\rho_f=\frac{M}{R_gT}P \tag{6}$$

Whereas, the solid phase density is constant.

2.2.2. Interphase momentum transfer coefficient

For porosities $\epsilon_f<0.80$, which might occur in the bottom section, the interphase momentum transfer coefficient β has been obtained from the well-known Ergun equation:

$$\beta=150\frac{(1-\epsilon_f)^2}{\epsilon_f}\frac{\mu_f}{d_p^2}+1.75(1-\epsilon_f)\frac{\rho_f}{d_p}|\bar{u}-\bar{v}| \tag{7}$$

whereas for porosities $\epsilon_f\geq 0.80$, the following expression for the interphase momentum transfer coefficient has been derived from the correlation of Wen and Yu [3]:

$$\beta=\frac{3}{4}C_{d,\,s}\frac{\epsilon_f(1-\epsilon_f)}{d_p}\rho_f|\bar{u}-\bar{v}|\,\epsilon_f^{-2.65} \tag{8}$$

In Eq. (8), the drag coefficient for a single particle $C_{d,\,s}$ depends on the particle Reynolds number Re_p as given by Schiller and Naumann [4]:

$$C_{d,\,s}=\begin{cases}\dfrac{24}{Re_p}+\dfrac{3.6}{Re_p^{0.313}} & Re_p<1000\\ 0.44 & Re_p\geq 1000\end{cases} \tag{9}$$

2.2.3. Friction between gas phase and tube wall

For the frictional pressure drop between the gas phase and tube wall the well-known Fanning relation [5] has been applied. Neglecting the influence of the particulate phase on the gas phase, the friction factor f_f appearing in the Fanning equation can be obtained from well-established empirical dimensionless correlations for single phase flow.

$$F_{f,\,wall}=-4f_f\frac{\epsilon_f}{D}\frac{1}{2}\rho_f u^2 \tag{10}$$

$$4f_f=C_1Re^{-C_2} \tag{11}$$

For very smooth tube walls and $2\times10^3<Re<10^5$, the Blasius relation [5] is valid with $C_1=0.316$ and $C_2=0.25$. If the tube wall roughness increases, the value of C_2 decreases, resulting in enhanced wall friction at the same average gas velocity.

2.2.4. Friction between solid phase and tube wall

To represent the frictional force per unit volume gas–solid mixture exerted by the tube wall on the solids phase, a modified Fanning relation is often used:

$$F_{s,\,wall}=-4f_s\frac{\epsilon_s}{D}\frac{1}{2}\rho_s v^2 \tag{12}$$

Unfortunately, no universal empirical relation exists for the friction factor f_s although several formulae have been proposed in the literature [6–12]. In most of these studies, discrepancies with respect to pressure gradient computed on basis of a simple axial model and experimental pressure drop data are attributed to friction between particles and the tube wall. Table 1 summarizes the empirical solid phase friction factor correlations previously presented in the literature, Table 2 the operating conditions for which they have been developed. The terms that have been neglected in the pressure drop analysis are also included in this table.

2.3. Numerical solution

The governing equations have been solved, together with the constitutive relations, using a fourth order Runge–Kutta numerical integration procedure with adjustable step size. Since in the computations the inlet pressure, and thereby the inlet density of the gas phase (through the ideal gas law), was chosen, the gas phase velocity required to attain a predefined gas phase mass flux was implicitly determined. Sim-

Table 1
Empirical correlations for the friction factor $4f_s$

Reference	Proposed relation for $4f_s$
Stemerding [6]	0.012
Reddy and Pei [7]	$\frac{0.184}{v}$
Capes and Nakamura [8]	$\frac{0.206}{v^{1.22}}$
Yang [10]	$A\frac{\epsilon_s}{(1-\epsilon_s)^3}\left[\epsilon_s\frac{Re_t}{Re_p}\right]^{-B}$
	$\frac{u}{v_t}<1.5$: $A=0.0410$, $B=1.021$
	$\frac{u}{v_t}>1.5$: $A=0.0126$, $B=0.979$
Kerker [9]	$\frac{3.13\times10^{-5}Ga^{0.26}}{217\epsilon_s+1}\left[\left(\frac{u_{sound}}{v}\right)^{1/2}\frac{D}{d_p}Ga^{0.16}\left(\frac{v^2}{gd_p}\right)^{-0.25}+1.55\times10^{-3}\left(\frac{u_{sound}^2}{gd_p}\right)^{1/2}\right]$
Breault and Mathur [12]	$\frac{48.8\epsilon_s}{v(1-\epsilon_s)^3}$

Table 2
Particle properties and operation conditions for the friction factors listed in Table 1

Reference	D (mm)	Solid material	d_p (μm)	u^0 (m s^{-1})	G_s (kg m^{-2} s^{-1})	Terms neglected in pressure drop analysis
Stemerding [6]	51	FCC	65	4–12		complete gas phase contribution
Reddy and Pei [7]	100	glass	100, 270	8–14	130–430	complete gas phase contribution
Capes and Nakamura [8]	75	glass, steel	300–3000	2.5–30		gravity forces acting on gas phase and acceleration of gas and solid phases
Yang [10]	7, 14, 27, 47, 76	glass, steel, copper, sand	100–3000			gravity forces acting on gas phase and acceleration of gas phase
Kerker [9]	83	glass	640	10–35	16.7–245	
Breault and Mathur [12]	38	sand, limestone	300, 452, 296	3.9–7.6		acceleration of both phases

ilarly the chosen value of the entrance solidity ϵ_s determines the initial axial solids velocity to satisfy a prescribed solids mass flux. These choices then influence the length of the acceleration zone.

3. Experimental

To study the effect of solid–wall friction in more detail, the CFB hydrodynamics have been studied in a stainless steel CFB unit, shown schematically in Fig. 1. In addition, the effect of elevated pressure on CFB hydrodynamics has been studied up to pressures of 6 bar.

Air has been used as the fluidizing agent in all experiments, and glass beads with diameters of 275 μm (ρ_s = 3060 kg m^{-3}) and 655 μm (ρ_s = 2900 kg m^{-3}) for the particulate phase. The glass beads were kept at incipient fluidization in a storage vessel (L = 1.20 m, D = 0.12 m) and were fed to the riser column through an inclined tube (L = 0.78 m, D = 0.030 m), mounted under an angle of 45° with respect to the riser column. The solids mass flow rate could be controlled with a slide valve, mounted halfway in the inclined connection tube. Fluidizing air to convey the glass beads was supplied at the bottom of the riser column (L = 3.0 m, D = 0.030 m). Just above the solids entry a solids distributor was included in the riser tube to achieve an uniform solids distribution over the tube cross-sectional area. This distributor was made of six staggered layers, each consisting of five pieces of 1.5 mm diameter steel wire positioned parallel to each other. At the exit of the riser column two cyclones separated the solids from the fluidizing air. After the second cyclone, the air left the system passing a throttle valve, whereas the solids were fed back to the storage vessel after having passed a weighing unit. The throttle valve made it possible to maintain a fixed pressure inside the CFB equipment.

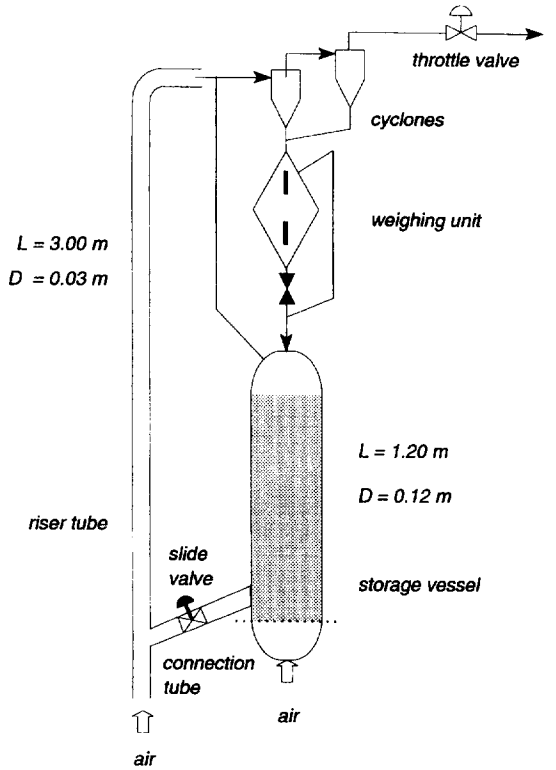

Fig. 1. Schematic representation of the circulating fluidized bed unit.

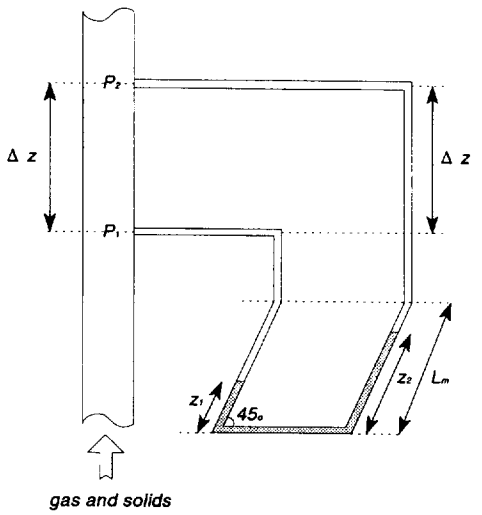

Fig. 2. Measurement of pressure drop over a riser section using water manometers.

In the axial direction, nine pressure taps were mounted in the wall of the riser column with an equidistant spacing of 34.5 cm. Pressure differences over these sections were measured using water manometers constructed of teflon tube ($D=6$ mm). To improve the accuracy of the pressure drop measurements these manometers were mounted under an angle of 45° with respect to the horizontal. In situations with small pressure drop, i.e. dilute flow conditions with low gas phase velocities, the hydrostatic pressure contribution of the gas phase present in the manometer tubes must be accounted for. The following relation for the pressure gradient ΔP over a section of the riser can be derived (see Fig. 2):

$$\frac{\Delta P}{\Delta z}=\frac{P_2-P_1}{\Delta z}=\rho_f g_z+\frac{z_2-z_1}{\Delta z}\sin(45°)(\rho_w-\rho_f)g_z \qquad (13)$$

The mass flow rate of the circulating solids could be determined by collecting the solids in the weighing vessel, during a certain period. Observation windows at the front and rear side of this vessel made it possible to observe the rate with which the solids content inside the vessel increases. Typically 4 kg of glass beads were collected from the total inventory of 24 kg, while the gas phase was bypassed to prevent pressure build up.

4. Results

4.1. Experimental

Prior to performing the two phase flow experiments, the pressure drop for single phase flow of air was measured as a function of gas velocity and operating pressure. The values of C_1 and C_2, defined by Eq. (11), were obtained from Fig. 3 which shows the pressure gradient as a function of Reynolds number. From this figure, the values of C_1 and C_2 were determined as respectively 0.0873 and 0.137. Following these single phase flow pressure drop measurements the gas–solid two phase flow was studied. In this figure, experimentally-determined pressure gradients were obtained at operating pressures of 1, 4 and 6 bars. Because the experiments were undertaken at the same gas mass flows, the experimental data overlap each other.

Fig. 4 shows the experimentally-determined pressure gradient as a function of height for three solids mass fluxes ($P=6$ bar, $u^0=48.8$ Nm s^{-1}, $d_p=275$ μm). (Note: Nm s^{-1} denotes 'normal metres per second', i.e. at ambient conditions of 1 bar and 293 K). Referring to Eq. (5), the solids acceleration with accompanying decrease in solids concentration, causes a strong decrease of the pressure gradient in the bottom region of the riser. At heights exceeding 1.5 m the pressure gradient equals the value corresponding to fully-developed flow, in which case wall friction and gravity forces completely dominate pressure drop. Assuming no change in the gas phase velocity profile due to the presence of particles, the friction between gas phase and tube wall causes a pressure

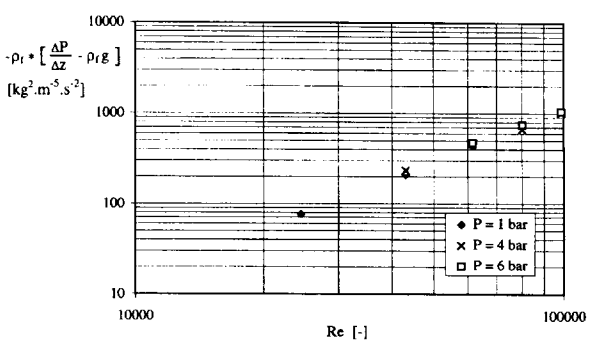

Fig. 3. Experimentally-determined pressure gradient vs. Reynolds number for single phase gas flow.

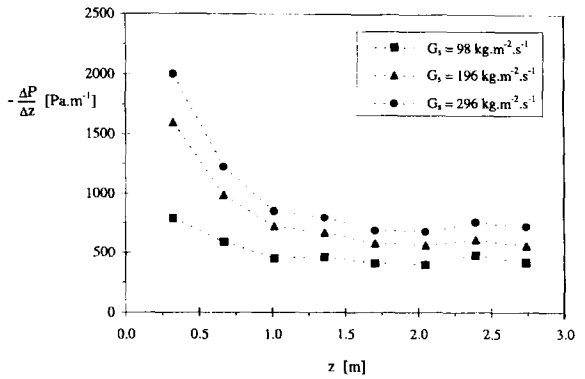

Fig. 4. Experimentally-determined pressure gradient as a function of height for three solids mass fluxes; $P=6$ bar, $u^0=48.8$ Nm s^{-1}, $d_p=275$ μm.

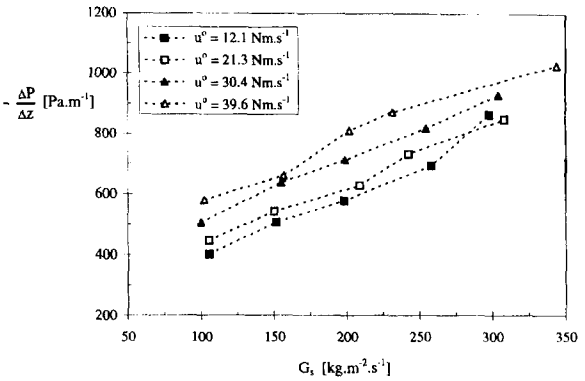

Fig. 5. Experimentally-determined pressure gradient as a function of solids mass flux for four gas velocities; $P=1$ bar, $d_p=655$ μm, $z=2.05$ m.

gradient of 140 Pa m^{-1} (see Fig. 3). Furthermore, the contribution due to gas phase hold-up equals 70 Pa m^{-1}. From Fig. 4 it can be concluded that for fully-developed two phase flow the gas phase is responsible for approximately 46% of the pressure gradient for the lowest solids mass flux of 98 kg m^{-2} s^{-1}. Even for the highest solids mass flux used ($G_s=296$ kg m^{-2} s^{-1}), the gas phase contributes for 28% to the pressure gradient.

Fig. 5 shows the experimentally-determined pressure gradient as a function of solids mass flux at 2.05 m above the solids entry for several gas velocities at atmospheric conditions ($d_p=655$ μm). The pressure gradient increases with increasing gas velocity, indicating pneumatic transport conditions. Additionally, the almost linear dependence of the pressure gradient with respect to the solids mass flux is noteworthy and will be considered in detail subsequently. At constant gas flow rate, changes in pressure gradient can only be attributed to contributions of the solids which, of course, depend on the solids mass flux. With respect to the solid phase contributions, one should realize that the solids hold-up changes linearly with solids mass flux, since for developed flow the solid phase velocity almost remains constant and equal to the difference between gas velocity and the particle terminal velocity as measured by Konno and Saito [13] for similar conditions. Since acceleration effects are minimal in the fully-developed flow regime, friction between solids and tube wall constitutes the remaining solids contribution to be considered. Moreover, it can be shown that solid phase acceleration effects would lead to a pressure gradient contribution that varies linearly with solids mass flux. As shown in Fig. 5, the total pressure gradient possesses a linear dependence with respect to solids mass flux and therefore the frictional contribution should vary either linearly with solids mass flux or remain constant. Thus, the solids friction factor (see Eq. (12)), is either independent of the solids mass flux or inversely proportional to this quantity.

Figs. 6 and 7 show similar results as depicted in Fig. 5, however, in these cases the operating pressures were 4 and 6 bar respectively. From the measurements obtained at an operating pressure of 4 bar (Fig. 6) it turned out that the pressure gradient first decreases with increasing gas velocity but for gas velocities exceeding 39.6 Nm s^{-1} (≈ 10 m s^{-1}) an increase in pressure gradient is found with increasing gas velocity. These observations indicate a transition from the fast fluidisation regime to the pneumatic transport regime. At a superficial gas velocity u^0 of 21.3 Nm s^{-1}, the riser operates in the fast fluidization regime and therefore the pressure gradient is more sensitive with respect to solids mass flux. The experiments obtained at $P=6$ bar (Fig. 7) show a constant decrease of pressure gradient with increasing gas velocity, at constant solids mass flux, indicating operation in the fast fluidization regime.

Fig. 8 shows the pressure gradient as a function of gas velocity for several operating pressures and a solids mass flux

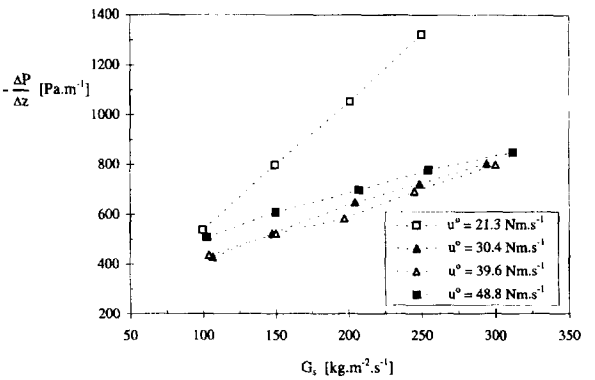

Fig. 6. Experimentally-determined pressure gradient as a function of solids mass flux for four gas velocities; $P=4$ bar, $d_p=655$ μm, $z=2.05$ m.

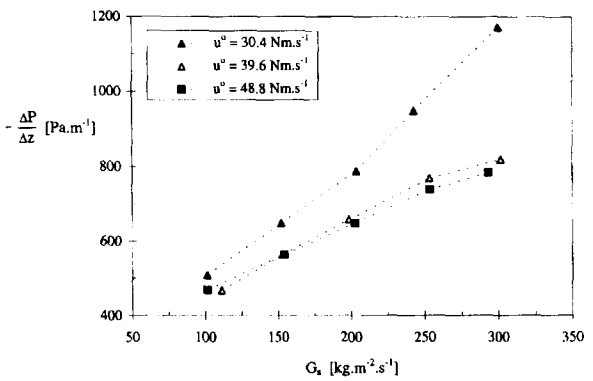

Fig. 7. Experimentally-determined pressure gradient as a function of solids mass flux for three gas velocities; $P=6$ bar, $d_p=655$ μm, $z=2.05$ m.

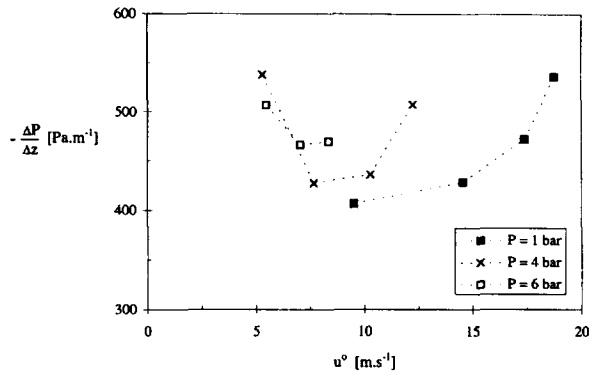

Fig. 8. Experimentally-determined pressure gradient as a function of gas velocity for three operating pressures; $d_p = 655$ μm, $G_s = 100$ kg m^{-2} s^{-1}, $z = 2.05$ m.

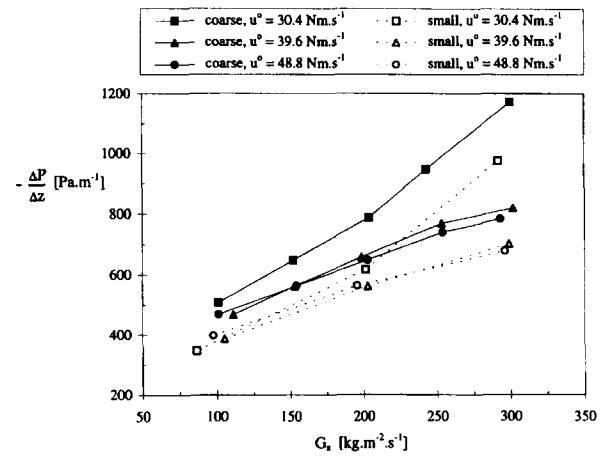

Fig. 9. Experimentally-determined pressure gradient as a function of solids mass flux for three gas velocities. Results are shown for small ($d_p = 275$ μm) and coarse ($d_p = 655$ μm) particles; $P = 6$ bar, $z = 2.05$ m.

of $G_s = 100$ kg m^{-2} s^{-1}. The experimental data obtained at atmospheric pressure again indicate operation in the pneumatic transport regime where the friction with the tube wall determines pressure drop, resulting in an increasing pressure gradient with increasing gas velocity. In contrast, at an operating pressure of 6 bar, the pressure gradient decreases with increasing gas velocity. This phenomenon is characteristic for operation in the fast fluidization regime, where gravity forces constitute the main contribution to pressure drop. For an operating pressure of 4 bar, first a decrease and subsequently an increase in pressure gradient is observed with increasing gas velocity, indicating a transition from fast fluidization to pneumatic transport regime.

Fig. 9 shows the pressure gradient as a function of solids mass flux for both small (275 μm) and coarse (655 μm) particles, and an operating pressure of 6 bar. From this figure it can be seen that the pressure gradient decreases with decreasing particle diameter. Small particles possess a relatively small terminal velocity, resulting in higher solid phase velocities for a given gas velocity. For a fixed solids mass flux this causes a decrease in solids concentration and therefore a decrease in pressure gradient. However, the friction between solids and tube wall will be augmented, causing an increase in pressure drop. Fig. 9 shows that of these competitive mechanisms the gravity forces constitute the dominant contribution to the total pressure gradient, resulting in a decrease in pressure gradient for decreasing particle sizes.

4.2. Model validation

Once a solids phase friction factor has been selected, the model equations, together with the constitutive relations can be solved. It turned out, however, that all friction factor relations listed in Table 1 predicted pressure gradients which considerably exceeded the experimentally-determined pressure gradients. In addition, the sensitivity of this quantity with respect to solids mass flux is overpredicted by these relations. These unsatisfactory results are probably due to the fact that most authors neglect the gas phase contribution. In the previous section it has already been shown that both gas phase wall friction and gas phase hold-up can contribute considerably to the total pressure gradient. The friction factor relation proposed by Kerker [9] possesses an almost inverse dependence with respect to solids mass flux and was able to predict correct pressure gradients at atmospheric conditions for gas phase velocities below 17 m s^{-1}. At higher gas velocities, and for higher operating pressures, the pressure gradients were significantly overestimated. For $P = 6$ bar the calculated pressure gradient is about 1.5 times the experimentally-determined pressure gradient for most operating conditions. Following Kerker, an empirical relation for the solid phase friction factor has been developed which is inversely proportional to the solids mass flux:

$$4f_s = \frac{7.0 \times 10^{-5} \rho_s v^{0.6}}{G_s} \tag{14}$$

This friction factor relation has been obtained by fitting the theoretically-predicted pressure gradient due to the particulate phase to its experimental counterpart. The latter quantity was obtained by subtracting the gas phase contribution, obtained from single phase flow pressure gradient measurements at the same gas velocity, from the experimentally-determined (total) pressure gradient.

Following this approach, it has been implicitly assumed that the gas phase velocity profile is relatively unaffected by the presence of the particulate phase.

Fig. 10 shows a comparison between theoretically-calculated and experimentally-determined pressure gradients as a function of height for three solids mass fluxes at an operating pressure of $P = 4$ bar. It may be clear that the model predictions are in good quantitative agreement with the experiments. At other conditions (i.e. other gas velocities and operating pressures) a similar degree of agreement was obtained as was the case for other gas phase velocities and operating pressures. Fig. 11 shows the contributions to total pressure gradient as a function of height for the indicated conditions. In this case the riser operates in the fast fluidization regime, resulting in a dominant role of the solids phase hold-up ($\epsilon_s \approx 1.5\%$). Furthermore, acceleration of the

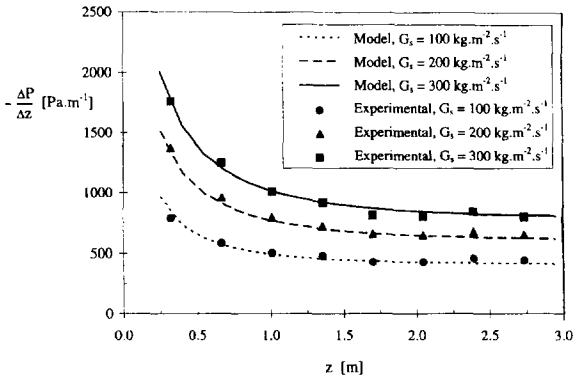

Fig. 10. Theoretically-calculated and experimentally-determined pressure gradient as a function of height for three solids mass fluxes; $P=4$ bar, $d_p=655$ μm, $u^0=2.05$ m.

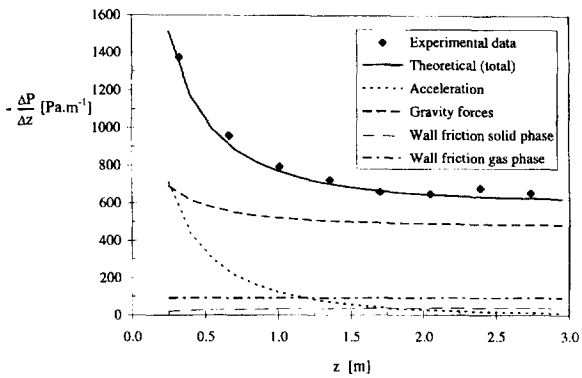

Fig. 11. Theoretically-calculated and experimentally-determined pressure gradient as a function of height. The contributions to the calculated pressure gradient are also shown; $P=4$ bar, $d_p=655$ μm, $u^0=7.7$ m s^{-1}, $z=2.05$ m.

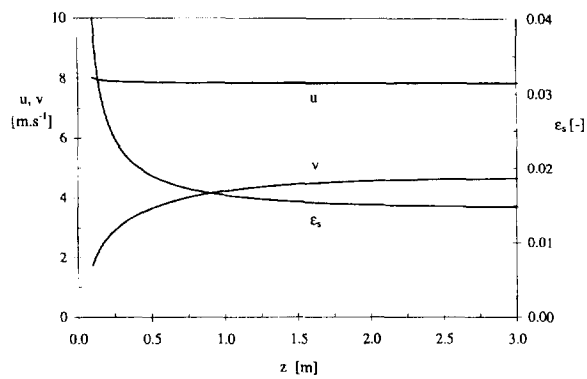

Fig. 12. Theoretically-calculated axial profiles of ϵ_s, u and v; $P=4$ bar, $d_p=655$ μm, $u^0=7.7$ m s^{-1}, $G_s=200$ kg m^{-2} s^{-1}.

solids causes a significant decrease in pressure gradient in the bottom region of the riser. Fig. 12 shows the axial velocity of both phases and solids concentration as a function of height ($P=4$ bar, $d_p=655$ μm, $u^0=30.4$ Nm s^{-1}, $G_s=200$ kg m^{-2} s^{-1}). From Fig. 12, it can be seen that the gas velocity is only slightly altered due to the presence of the solid phase. The solid phase velocity increases in the bottom region until a slip velocity is reached which approximately equals the terminal velocity of the particles studied ($v_t=3$ m s^{-1}).

Figs. 13, 14 and 15 compare calculated and experimentally-determined pressure gradients as a function of solids

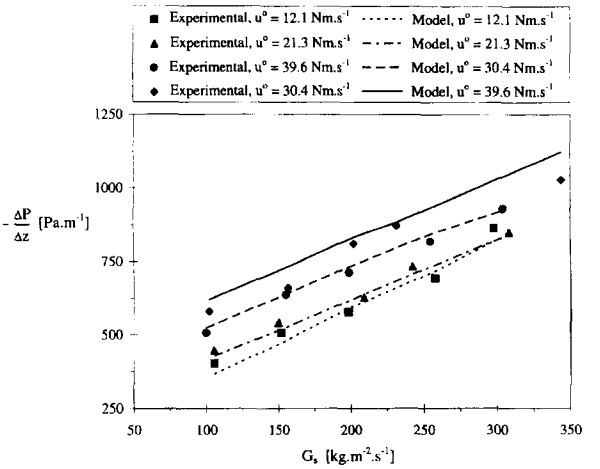

Fig. 13. Theoretically-calculated and experimentally-determined pressure gradient as a function of solids mass flux for several gas phase velocities; $P=1$ bar, $d_p=655$ μm, $z=2.05$ m.

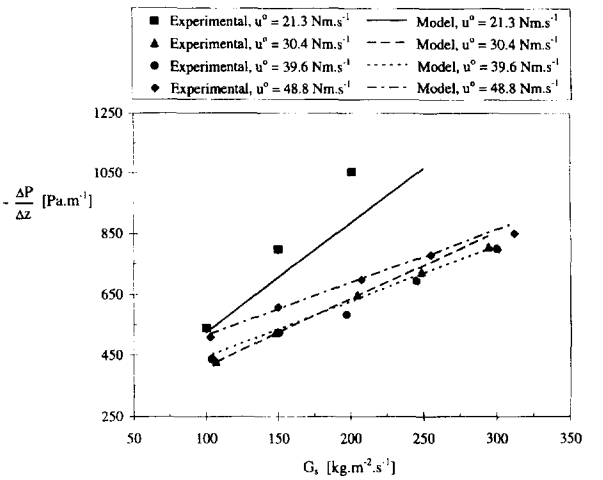

Fig. 14. Theoretically-calculated and experimentally-determined pressure gradient as a function of solids mass flux for several gas phase velocities; $P=4$ bar, $d_p=655$ μm, $z=2.05$ m.

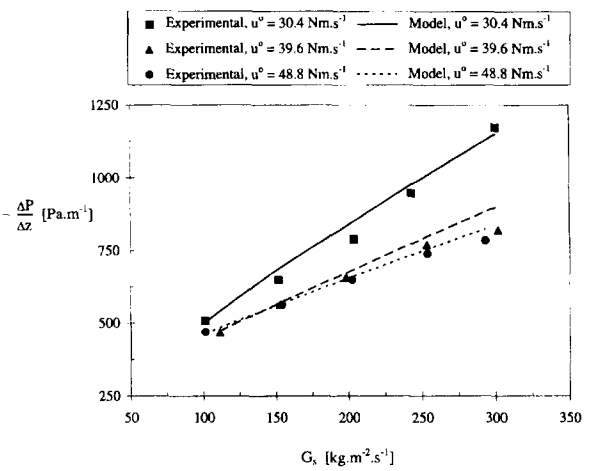

Fig. 15. Theoretically-calculated and experimentally-determined pressure gradient as a function of solids mass flux for several gas phase velocities; $P=6$ bar, $d_p=655$ μm, $z=2.05$ m.

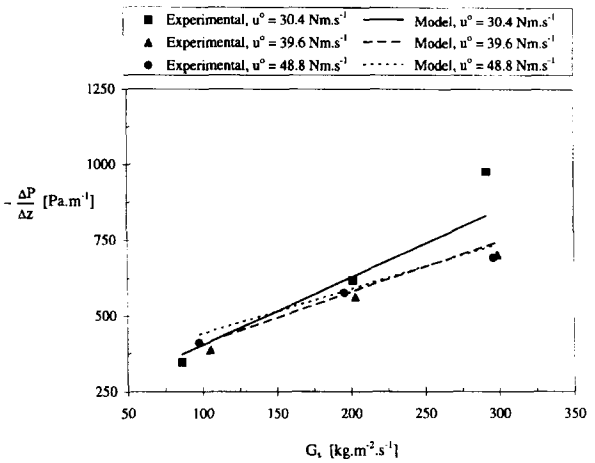

Fig. 16. Theoretically-calculated and experimentally-determined pressure gradient as a function of solids mass flux for several gas phase velocities; $P=6$ bar, $d_p=275$ μm, $z=2.05$ m.

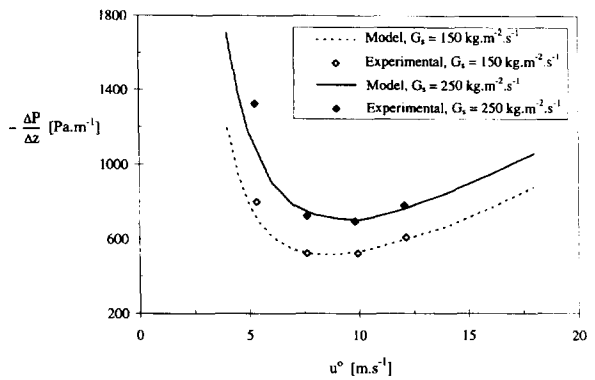

Fig. 17. Theoretically-calculated and experimentally-determined pressure gradient as a function of gas velocity for two different solids mass fluxes; $P=4$ bar, $d_p=655$ μm, $z=2.05$ m.

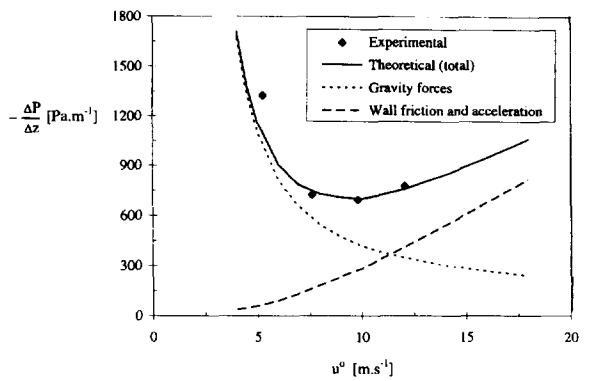

Fig. 18. Theoretically-calculated and experimentally-determined pressure gradient as a function of gas velocity; $P=4$ bar, $G_s=250$ kg m^{-2} s^{-1}, $d_p=655$ μm, $z=2.05$ m.

mass flux for several gas velocities at operating pressures of 1, 4 and 6 bar respectively. The theoretical results are generally in satisfactory agreement with the experimental data, except for the lowest gas velocity $u^0=21.3$ Nm s^{-1} at $P=4$ bar. Here the calculated pressure gradient underestimates the experimentally-determined pressure gradient significantly. Because the solids concentration is approximately 5% this discrepancy might be due to cluster formation, radial segregation of solids and solids downflow near the tube wall, phenomena which have frequently been observed in dense systems [14]. These phenomena tend to increase the solids hold-up inside the riser tube and are not accounted for in the present model. Fig. 16 demonstrates the applicability of the friction factor Eq. (14) for small particles (275 μm) at an operating pressure $P=6$ bar. Only the experimentally-determined pressure gradient for $u^0=5$ m s^{-1} and $G_s=300$ kg m^{-2} s^{-1} is underestimated by the model which probably can be related to the aforementioned phenomena.

Fig. 17 shows the pressure gradient versus gas velocity for two solids mass fluxes and demonstrates the ability of the model to predict the correct transition velocity between the fast fluidization regime and the pneumatic transport regime. For the solids mass flux of 250 kg m^{-2} s^{-1} the calculated contributions due to gravity forces, wall friction and acceleration are shown in Fig. 18. It may be clear that below $u^0=6$ m s^{-1} the solids hold-up dominates the total pressure gradient. For gas velocities exceeding 15 m s^{-1} wall friction becomes more important, although the solids hold-up is still responsible for a noticeable contribution to the pressure gradient.

5. Conclusions

A simple one-dimensional engineering model has been developed to describe riser hydrodynamic key variables in axial direction. Model predictions have been compared with experimental data obtained for two particles sizes ($d_p=655$ μm, $\rho_s=2900$ kg m^{-3}; $d_p=275$ μm, $\rho_s=3060$ kg m^{-3}) in a riser tube ($L=3$ m, $D=0.03$ m) which could be operated at a maximum pressure of 6 bar.

At low gas velocities, the riser operated in the fast fluidization regime, where solids hold-up is the dominant contribution to pressure gradient. Upon increasing the gas velocity at constant solids mass flux a decrease in pressure gradient was found. At high gas velocities the dominant contribution to the pressure gradient is friction of both phases with the tube wall. This corresponds to operation in the pneumatic transport regime where an increase in gas velocity results in increasing pressure gradient. The pressure gradient proved to be proportional to solids mass flux G_s at a fixed gas velocity, which implies that f_s is either constant or varies reciprocally with G_s.

None of the empirical correlations for the solids friction factor f_s presented in literature led to a satisfactory prediction of the experimental data. Therefore a new solids friction factor correlation has been developed, which possesses a reciprocal dependence with respect to solids mass flux. Using this friction factor, the hydrodynamic model predicted pressure gradients which were in good agreement with experimental data for several operating pressures, gas velocities, solids mass fluxes and particles sizes. Even the transition velocity between the fast fluidization regime and the pneu-

matic transport regime could be predicted correctly. The model has been used to obtain more knowledge concerning the contributions to total pressure gradient in the aforementioned regimes of operation.

6. List of symbols

C	constants defined in Eq. (11) (–)
$C_{d,s}$	drag coefficient for an isolated particle (–)
D	tube diameter (m)
d_p	particle diameter (m)
F	force per unit volume (kg m^{-2} s^{-2})
f	friction factor (–)
G_s	mass flux (kg m^{-2} s^{-1})
g_z	gravitational force per unit mass (m s^{-2})
L	tube length (m)
M	molecular mass (kg mol^{-1})
P	pressure (kg m^{-1} s^{-2})
R_g	universal gas constant (kg m^2 s^{-2} mol^{-1} K^{-1})
T	temperature (K)
u	gas phase velocity in axial direction (m s^{-1})
u^0	superficial gas phase velocity (m s^{-1})
u_{sound}	sonic single phase velocity (m s^{-1})
v	solid phase velocity in axial direction (interstitial) (m s^{-1})
z	axial coordinate (m)

Greek letters

β	interphase momentum transfer coefficient (kg m^{-3} s^{-1})
ϵ	volume fraction (–)
μ	shear viscosity (kg m^{-1} s^{-1})
ρ	density (kg m^{-3})

Subscripts

f	fluidum
p	particle
s	solid phase
t	terminal
w	water
wall	tube wall

Dimensionless groups

Ga	Galileo number $\frac{\lvert g\rvert d_p^3 \rho_f(\rho_s-\rho_f)}{\mu_f^2}$
Re	Reynolds number $Re=\frac{\rho_f U D}{\mu_f}$
Re_p	Particle Reynolds number $Re_p=\frac{\rho_f \epsilon_f \lvert\bar{u}-\bar{v}\rvert d_p}{\mu_f}$

Acknowledgements

This investigation was financially supported by Koninklijke Shell Laboratorium Amsterdam (KSLA). The authors also acknowledge L.J.H. ter Bogt for his contribution to the model development, G. Schorfhaar for his technical support and M. Lommers for his support in obtaining the experimental data.

References

[1] J.A.M. Kuipers, H. Tammes, W. Prins and W.P.M. van Swaaij, *Powder Technol., 71* (1992) 87.
[2] J. Yerushalmi and A.A. Avidan in J.F. Davidson and D. Harrison (eds.), *Fluidization*, Academic Press, New York, 2nd edn., 1985, p. 225.
[3] Y.C. Wen and Y.H. Yu, *Chem. Eng. Prog. Symp. Ser., 62* (1966) 100.
[4] L. Schiller and A. Naumann, *Z. Ver. Dtsch. Ing., 77* (1935) 318.
[5] R.B. Bird, W.E. Stewart and E.N. Lightfoot, *Transport Phenomena*, Wiley, New York, 1960.
[6] S. Stemerding, *Chem. Eng. Sci., 17* (1962) 599.
[7] K.V.S. Reddy and D.C.T. Pei, *Ind. Chem. Eng. Fundam., 8* (1969) 490.
[8] C.E. Capes and K. Nakamura, *Can. J. Chem. Eng., 51* (1973) 31.
[9] L. Kerker, *Ph.D Dissertation*, University of Karlsruhe, Karlsruhe, Germany.
[10] K. Nakamura and C.E. Capes, *Can. J. Chem. Eng., 51* (1973) 39.
[11] W.C. Yang, *AIChE J., 24* (1978) 548.
[12] R.W. Breault and V.K. Mathur, *Ind. Eng. Chem. Res., 28* (1989) 684.
[13] H. Konno and S. Saito, *J. Chem. Eng. Jpn., 2* (1969) 211.
[14] J.J. Nieuwland, P. Huizenga, J.A.M. Kuipers and W.P.M. van Swaaij, *Chem. Eng. Sci., 49* (1995) 5803.